A MULTI-PHYSICS FINITE ELEMENT MODEL FOR THE CRASHWORTHINESS OF ELECTRIC VERTICAL TAKE-OFF AND LANDING AIRCRAFT AND ITS LITHIUM-ION BATTERY: A PRELIMINARY STUDY

Luca Riva
Politecnico di Milano
Milan, Italy

Alessandro Giustina
Politecnico di Milano
Milan, Italy

Marco Anghileri
Politecnico di Milano
Milan, Italy

Stefano Dolci
Center for Collision
Safety and Analysis
George Mason University
Fairfax, VA, United States

Cing-Dao Kan
Center for Collision
Safety and Analysis
George Mason University
Fairfax, VA, United States

Leyu Wang*
Center for Collision
Safety and Analysis
George Mason University
Fairfax, VA, United States

ABSTRACT

Electric Vertical Take-Off and Landing (eVTOL) aircraft are laying the foundations for Advanced Air Mobility (AAM), which represents a fundamental shift in how short-range air transportation is conceived and implemented. Compared to aircraft powered by internal combustion engines, eVTOLs present innovative configurations due to their use of electric propulsion systems and Lithium-Ion battery for energy storage. These differences require regulatory agencies to develop new crashworthiness standards for this category, that address both occupants' safety and the potential risk associated with the battery thermal runaway. This preliminary study aims to create a high-fidelity Finite Element model to analyze the crashworthiness of eVTOLs and their battery. The geometry and configuration selected feature a fixed-wing tiltrotor design. The expected aircraft performance metrics are estimated, including range, mean cruise speed, maximum take-off mass and system nominal voltage. A multi-physics analysis is necessary to study how battery placement affects crash safety, reflecting typical eVTOL design choices. Three battery placement configurations are being evaluated, with the battery pack installed above the subfloor in the cabin, behind the passengers, or embedded within the wing structure. This paper discusses the first case, including the complete development of multi-physics Finite Element models for the battery pack and the subfloor, and the evaluation of its battery crash-stability performance during emergency landing on hard surfaces. The simulation framework developed offers a viable approach for achieving design-through-analysis in the regulation compliance for eVTOL crashworthiness design.

NOTATION

*

Symbols

A Cell Surface Area, m^2

$C3$ Double Layer Capacitor, mF

i Electric Current, A

l Resistance thickness, m

M_{TOM} Maximum Take-Off Mass, kg

$P_{\mathbf{batt}}$ Battery Power, W

$P_{\mathbf{batt,res}}$ Battery Power Reserve, W

$P_{\mathbf{cr}}$ Cruise Power, W

$R11$ Electrolyte Solution Resistance, $\mu\Omega$

$R2$ Charge Transfer Resistance, $\mu\Omega$

$R_{eq,Mod0}$ *Module 0* Equivalent Resistance, Ω

$R_{eq,ModA}$ *Module A* Equivalent Resistance, Ω

R_EXT External Resistance, Ω

$R_{\mathbf{int,total}}$ Internal Total Resistance, mΩ

SH Specific Heat, J/(kg K)

∗ Corresponding author

TC Thermal Conductivity, W/(m K)

$V1$ Battery Cell Voltage, V

$V_{\mathbf{batt}}$ Battery Voltage, V

$v_{\mathbf{c}}$ Cruise Speed, km/h

$V_{\mathbf{EXTRES}}$ External Resistor Voltage Drop, V

V_{module} Battery Module Voltage, V

$V_{total,pack}$ Battery Pack Voltage, V

ρ Electrical Resistivity, Ω

σ Electrical Conductivity, S/m

σ_{cat} Cathode Electrical Conductivity, S/m

σ_Y Yield Stress, MPa

*

Acronyms

AMC / MOC Acceptable Means of Compliance

CAD Computer Aided Design

CCSA Center for Collision Safety and Analysis

CoG Center of Gravity

EASA European Union Aviation Safety Agency

ESS Energy Storage System

eVTOL electric Vertical Take-Off and Landing

FAA Federal Aviation Administration

GND Ground

SC Special Condition

TLAR Top-Level Aircraft Requirement

UAM Urban Air Mobility

VTOL Vertical Take-Off and Landing

INTRODUCTION

The aerospace industry has experienced significant changes over the past fifteen years, driven by numerous innovations in aircraft designs oriented towards an increment of frequent short-range flights. A new category of aircraft, known as electric Vertical Take-Off and Landing (eVTOLs), is starting replacing traditional combustion engines by substituting them with electric battery or fuel cell systems. eVTOLs are establishing the basis for Advance Air Mobility (AAM), a new infrastructure framework focused on short-range flights in congested areas, referred to as Urban Air Mobility (UAM), as well as on intercity connections, known as Regional Air Mobility (RAM). Various eVTOL configurations have been developed in recent years; *Multicopters* generate lift and thrust entirely from rotors without presenting any fixed lifting surface, and operate similarly to helicopters. *Lift + Cruise* configurations use dedicated rotors for vertical take-off and landing and a separate propulsion propeller for forward flight, added to a fixed wing to generate lift during cruise. *Tiltrotors* and *Tiltwing* designs feature either the rotors or the entire wing to rotate, allowing the propulsion system to provide lift during vertical take-off and landing, and forward thrust during cruise flight. Other configurations include *Ducted fans with vectored thrust*, where propellers are embedded in the wing structure (Ref. 1). A typical eVTOL flight mission profile involves a vertical take-off, a cruise phase, and a vertical landing on a helipad. *Tiltrotors* and *Lift + Cruise* aircraft are the most exploited configurations due to their range and payload performance. The distributed electric propulsion used for most eVTOL designs also enhances safety margins in the event of a rotor failure.

Despite the progress, a limited operational experience hinders the development of eVTOL safety regulations. A deeper understanding regarding the aircraft battery safety is necessary for establishing comprehensive safety standards for this category of aircraft.

This work investigates the behavior of the battery during an eVTOL vertical hard landing. Three battery placement configurations are being analyzed: battery installed on the subfloor, battery located behind the passenger, and battery embedded within the wings structure. This paper presents the first case, where the battery is set on the subfloor, including the development of multi-physics finite element model for the battery pack and subfloor, and the evaluation of battery safety performance during emergency landing on hard surfaces. A generic eVTOL CAD model with tilted rotor configuration was designed using SolidWorks, as shown in Figure 1.

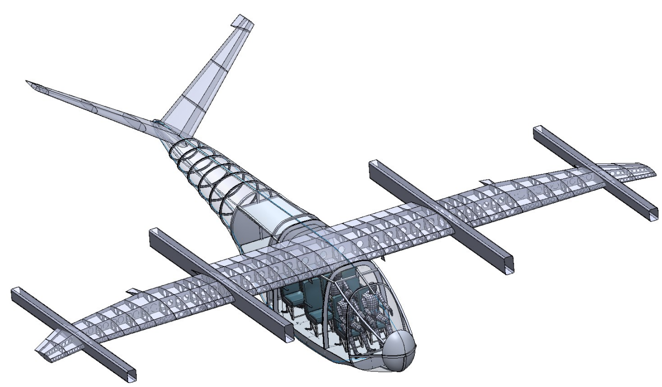

Figure 1. Demonstrator CAD.

Battery Regulations for eVTOL

To the authors best knowledge, there is not a unified univocal regulation that clearly defines the safety requirements for the

Energy Storage Systems (ESS) used in eVTOL propulsion. Both EASA and the FAA are currently moving towards a formal definition of the eVTOL aircraft category, although their approaches still manifest minor differences.
The first edition of *Special Condition for small-category VTOL-capable aircraft* was published by EASA in July 2019 (Ref. 2), with an update released in June 2024 (Ref. 3). The document does not explicitly refer to electric propulsion systems as the main driver for VTOL propulsion, although it is often considered the key reference for all eVTOL designs. On the other hand, the FAA has introduced a category called *Powered-Lift* (Ref. 4), which follows a similar regulatory path. Regarding battery operational safety, thermal runaway and battery fires are considered the most critical events, as they may occur in any flight phase, including ground operations when the motors are not powered. To mitigate those risks, fire-isolation criteria have been defined to allow the occupants to safely evacuate the cabin under any emergency condition. *VTOL.2325* (Ref. 2) states: *"aircraft must be designed to minimize the risk of fire initiation due to anticipated heat or energy dissipation [...] that are expected to generate heat sufficient to ignite a fire; [enabling] a survivable emergency landing"*. Additionally, *VTOL.2430* (Ref. 2) emphasizes that *"each system must be designed to provide independence between multiple energy storage and supply systems so that a failure, including fire, [...] will not result in the loss of energy storage"*. These statements highlight that fire conditions are expected to happen and may occur also during flight, so proper thermal isolation of the ESS becomes mandatory. Several regulations related to battery safety in crash scenarios have already been defined; however, uncertainties remain regarding their effective applicability and consistency in the eVTOL field. Ongoing research efforts in both Europe and the United States are focused on validating new guidelines and protocols relevant to this issue. Experts from NASA, the FAA and private industry are collaborating to develop coherent Acceptable Means of Compliance (AMC) aligned with the current battery technology and operational experience.

NASA Langley Research Center conducted a detailed analysis of all the active regulations concerning ESS undergoing dynamic testing (Ref. 5). Their work aimed to identify a test method that can serve as a certification basis and potentially be extended as a broader certification reference, keeping into account all the *"unknowns associated with the survivability of the ESS in a dynamic mishap event or crash"* (Ref. 5). A key finding of this research is that, although aircraft standards for ESS exist, none were written specifically for aircraft that use batteries or electric propulsion as the primary power source.
MOC SC-VTOL-issue-2 in *MOC VTOL.2325(a)(4) Fire Protection - Energy storage crash resistance* describes the EASA current drop test procedure (Ref. 3): the battery must be dropped from a height of at least 15.2 meters (50 feet) on a rigid, non-deforming surface. The ESS should be charged or filled to its most critical expected state during a crash, and released in an orientation representative of its typical installation onboard, impacting in a horizontal position within ±10° of the aircraft's longitudinal axis. After the impact, there should be no risk of post-crash fire or other harmful gas emissions within a time frame compatible with the rescue of seriously injured occupants. On the other hand, with regard to FAA regulations, no special rules currently exist that address electric systems as the primary propulsion source. Nonetheless, both European and U.S. authorities are working toward harmonized regulations. For this reason, all U.S. developers are aligning with current *EASA* standards. Therefore, *EASA* criteria were adopted as a reference for the drop test requirements.
The major hazards identified during battery crash scenarios include off-gassing (i.e., gas leakage) and thermal runaway. Thermal runaway occurs when a battery cell's internal temperature increases uncontrollably, typically due to internal short circuits caused by failure of the battery separator film, leading to a rapid self-accelerated heating and, potentially, fire. This phenomenon is generally observed when internal temperatures inside batteries reach approximately 140-160°C. Figure 2 illustrates the thermal runaway sequence of a Lithium-Ion battery.

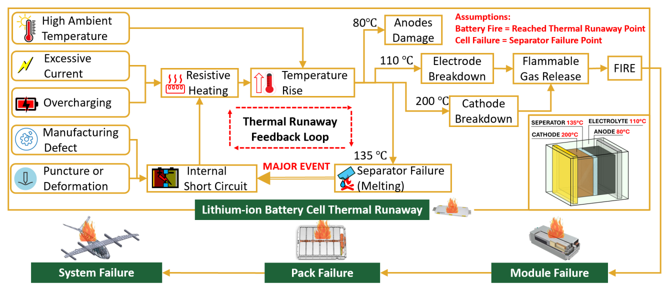

Figure 2. Battery thermal runaway phenomenon.

A triggering event, such as a structural deformation or a manufacturing defect, can induce an internal short circuit within the battery cell, leading to a rapid temperature rise. Once the cell temperature exceeds the melting point of the plastic separator film, additional internal short circuits may develop and propagate. This self-sustained positive feedback loop escalates into a battery cell thermal runaway event. The failure of a single cell starts acting as a heat source, triggering thermal runaway in neighboring cells and eventually leading to the failure of the entire battery pack. The flammable gases released during this process may ignite upon contact with oxygen, which further accelerates the process.
The objective of this study is to understand the consequences of installing battery packs in different locations of the eVTOL, aiming at deriving insights that can help developing the future eVTOL regulatory crashworthiness criteria. Hence, a multiphysics analysis framework is proposed to simulate the battery thermal runaway of the battery installed in the eVTOL airframe during a crash event.

METHODOLOGY

eVTOL Design and Performance

The demonstrator's *Top Level Aircraft Requirements (TLARs)* define the main operational targets to be achieved during the conceptual design phase. These include parameters such as total mass, flight endurance, range and system voltage. Our selected eVTOL *TLAR*s are summarized in Table 1.

Table 1. eVTOL *TLAR*s.

TLAR parameters	Reference value
Maximum take-off mass	4 000 kg (8 820 lbs)
Maximum payload mass	800 kg (1 760 lbs)
Expected battery pack mass	1200 kg (2 650 lbs)
Passengers	8
Configuration	Tiltrotor
Cruise speed v_c	250 km/h
Absolute ceiling	2000 m
Required range	120 km
Time of flight	>30 min
Battery cell capacity	78 Ah
System voltage	800 V

M_{TOM} exceeds the upper limit established in the first edition of the *SC-VTOL* (Ref. 2) regulation issued by *EASA* in 2019, while it respects the second edition criteria (Ref. 3). This choice is justified by a gap in the current state-of-the-art market, where most aircraft design accommodate no more than five passengers.
Based on internal performance analyses, the estimated operational range for our eVTOL is 140.2 km (75% of the battery total capacity), which increases to 211.6 km, when accounting for the additional 25% energy reserve. As a result, a mass of 1 232 kg has been allocated for the ESS, which is slightly heavier the *TLAR* hypothesized value; however, the percentage ratio between the ESS mass and the total aircraft mass is consistent with values observed in eVTOL designs that are already in advanced stages of development.

Battery Cell Numerical Model

The *NCM712 LGX E78* (Ref. 6) Lithium-Ion cell was selected off-the-shelf to be the baseline unit for the entire battery pack. This choice ensures compatibility with commercially available technologies. Each cell presents a mass of 1.07 kg, including its external protective pouch bag, and provides a nominal voltage of 3.7 V, which is assumed constant in first approximation.
According to available datasheets (Ref. 7), the cell offers an energy density of 259.0 Wh/kg. This value decreases to 226.8 Wh/kg when accounting for the external battery module case and internal circuitry.
A detailed numerical representation of the cell was developed with nonlinear FE software *LS-DYNA*, presenting all its layers internal thicknesses, densities and electrical and thermal properties. The cell's internal layout is shown in Figure 3, with the layer thicknesses visually multiplied by four for a sake of clarity. All the cells present a longitudinal section of 98.0 mm × 501.6 mm.
The original components within the battery cell comprise multiple layers of very thin membranes. A representative model is thus necessary to simplify the geometry in order to avoid excessive computational effort. Its dimensions and materials are reported in Table 2. Each representative cell model is composed of 5 distinct layers: an aluminum cathode current collector, a Lithium-Cobalt-Oxide cathode layer; a permeable polyethylene separator; a graphite anode layer; and a copper anode current collector. The cathode and the cathode current collector share the nodes on one face, and so do the anode and anode current collector. The separator in the middle is constrained with a frictional contact to the other layers of the cell.

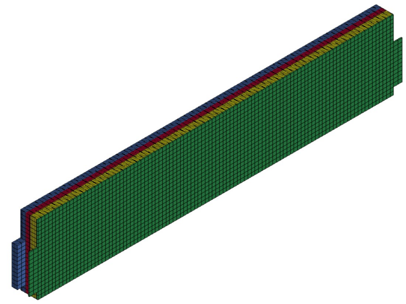

Figure 3. Battery cell model internal layers.

Table 2. Cell's geometric and material properties.

Layer	Color	Material	Th. [mm]
Cathode coll.	Green	Al	0.476
Cathode	Yellow	$LiCoO_2$	2.868
Separator	Brown	HDPE	0.379
Anode	Red	Graphite	1.932
Anode coll.	Blue	Cu	2.530

Table 3 collects the internal electric and thermal coefficients implemented in the numerical model.

Table 3. Cell's electric conductivity σ, specific heat SH, and thermal conductivity TC.

Layer	σ [$\frac{S}{m}$]	SH [$\frac{J}{kg \cdot K}$]	TC [$\frac{W}{m \cdot K}$]
Cathode coll.	3.77E7	900	210
Cathode	1.00E4	715	5.4
Separator	1.00E-8	1900	0.44
Anode	2.50E5	718	155
Anode coll.	5.96E7	385	385

All the electric conductivity values come from internal CCSA reports (Ref. 8). Among these parameters, the electric conductivity of the cathode layer σ_{cat} required special consideration. While the experimentally measured value is approximately 0.01 S/m, a significantly higher value was adopted in the simulation model. This discrepancy is caused by the representative modeling approach adopted, in which multiple thin anode and cathode layers present in a real cell are approximated by using a reduced number of thicker layers. When the electric current flows through the thickness direction of multiple thin plates connected in parallel, the circuit exhibits lower resistance compared to the case where current passes through the stacked thin layers connected in series.

Assume an electrical circuit composed of N identical resistors r_p, connected in parallel. The equivalent resistance R_p is given by Equation (1):

$$\frac{1}{R_p} = \underbrace{\frac{1}{r_p} + \frac{1}{r_p} + \cdots + \frac{1}{r_p}}_{N \text{ resistors}} = \frac{N}{r_p}, \quad \Rightarrow \quad R_p = \frac{r_p}{N} \tag{1}$$

Now consider a second electrical circuit composed of N identical resistors r_s, connected in series. In this case, the equivalent resistance R_s can be expressed as in Equation (2):

$$R_s = \underbrace{r_s + r_s + \cdots + r_s}_{N \text{ resistors}}, \quad \Rightarrow \quad R_s = N r_s \tag{2}$$

Since both systems are built from the same fundamental resistor unit, r_p and r_s must be equivalent. By isolating r_s, Equation (2) becomes:

$$r_s = \frac{R_s}{N} \tag{3}$$

By substitution, the relationship between the equivalent resistors becomes:

$$R_p = \frac{R_s}{N^2} \tag{4}$$

Recalling that resistance is related to material resistivity according to Equation (5):

$$R = \frac{\rho l}{A}, \tag{5}$$

and assuming all resistors share the same geometry, the resistivity ρ_p associated with the parallel configuration can be expressed as:

$$\rho_p = \frac{\rho_s}{N^2} \tag{6}$$

Since conductivity σ is defined as the reciprocal of resistivity, the final relationship reads:

$$\sigma_p = \sigma_s N^2 \tag{7}$$

In conclusion, when transitioning from a parallel to a series configuration, the conductivity must be scaled by a factor of N^2 to preserve the equivalence with the original total resistance. According to internal data, the *NCM712 LGX E78* Lithium-Ion cell consists of 23 cathode and anode layers, meaning that $N = 23$. As a result, the effective resistivity ρ decreases, while the corresponding conductivity σ rises up.

However, the cathode layer exhibits the lowest σ value among the conductive layers, indicating it is the main contributor to the internal voltage drop, as presents a conductivity coefficient which is orders of magnitude lower than the other layers. A precise estimation of the effective numerical σ_{cat} was obtained through iterative trial-and-error simulations of the cell's conductivity, calibrated with our in-house experimental measurements on the cell internal resistance.

To improve the fidelity of the mechanical–electrical–thermal coupled model, the battery internal resistance and capacity effects are modeled using a simplified Randles circuit, represented in Figure 4, to account for the cell's intrinsic voltage drop.

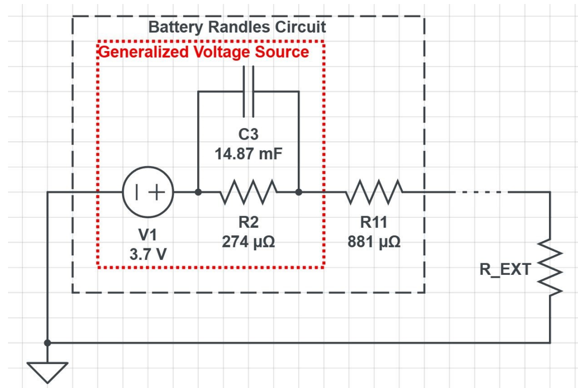

Figure 4. Simplified Randles Cell. (Ref. 9)

This simplified model is composed of two resistors and one capacitor but does not include the Warburg element, which accounts for the diffusion processes in dielectric spectroscopy.

The red window describes the generalized voltage source used in the simulation. V1 sets the cell's voltage, while C3 represents the double-layer capacitor and R2 the polarization resistance (also called charge transfer resistance). The double layer capacitor effect manifests at the electrode/electrolyte interface, where opposite charges - electrons on the electrode and ions in the electrolyte - are separated by a thin solvent layer acting as a dielectric in a conventional capacitor. The stored charge depends on the voltage applied by V1. R2 represents the resistance faced by ions moving from the electrolyte to the electrode, a phenomenon known as activation polarization. Additionally, R11 represents the electrolyte solution resistance. To conclude, a dashed line on the right side virtually symbolizes all the other cells of the battery pack, while *R_EXT* simulates the external resistance.

The R11 ($0.881 m\Omega$) and R2 ($0.276 m\Omega$) values are obtained from an internal tests results at Center for Collision Safety and Analysis (CCSA). R11 is characterized by a value at least three times larger than R2, so it affects with a greater impact the voltage drop. In LS-Dyna, the Randles battery model is implemented using **DEFINE_FUNCTION* cards to replicate R2 and C3, while R11 is mainly influenced by the conductivity values reported in Table 2. In this preliminary study the variations of the resistivity caused by the change of temperature and state of charge have been neglected. The resistivity change due to geometric deformations will be reflected as the change of R11. It has to be noted that R11 is calculated by the finite element solver in real time based on the cell geometry and the electric conductivity of the cell's materials.

Two Types of Battery Modules: *Module 0* and *Module A*

Two battery modules with different dimensions and number of cells have been developed, referred to as *Module 0* and *Mod-*

ule A, in order to meet the constraints on the percentage of the M_{TOM} allocated to the ESS, as well as the nominal voltage defined in the *TLAR*s (Table 1). Performance studies revealed that, in order to meet the required performance targets with a unique battery module, a larger number of batteries would have been necessary if compared to initial estimates. Additionally, employing battery modules of different shapes enables a more efficient integration and installation within the aircraft structure, and the use of multiple modules allows also for a preliminary evaluation of the advantages and disadvantages of employing smaller modules with equivalent voltage drop. Their final shape and dimensions become a direct outcome of preliminary placement studies aimed at optimizing their installation within the aircraft. The two designs are now discussed.
The first battery module, *Module 0*, consists of 36 cells organized in a 3p12s (three parallel, twelve series) configuration. Its nominal voltage is $3.7 \times 12 = 44.4\,\text{V}$. Figure 5 shows its internal circuitry, outlined by a red dashed line. To reduce the computational effort, 12 cells in a 3p4s configuration were merged into a single representative cell, preserving its original designed layers. The new unit is called *Lot 0* and it is graphically delimited by a dashed black line. As a result, *Module 0* is composed of 3 *Lots 0* connected in series.

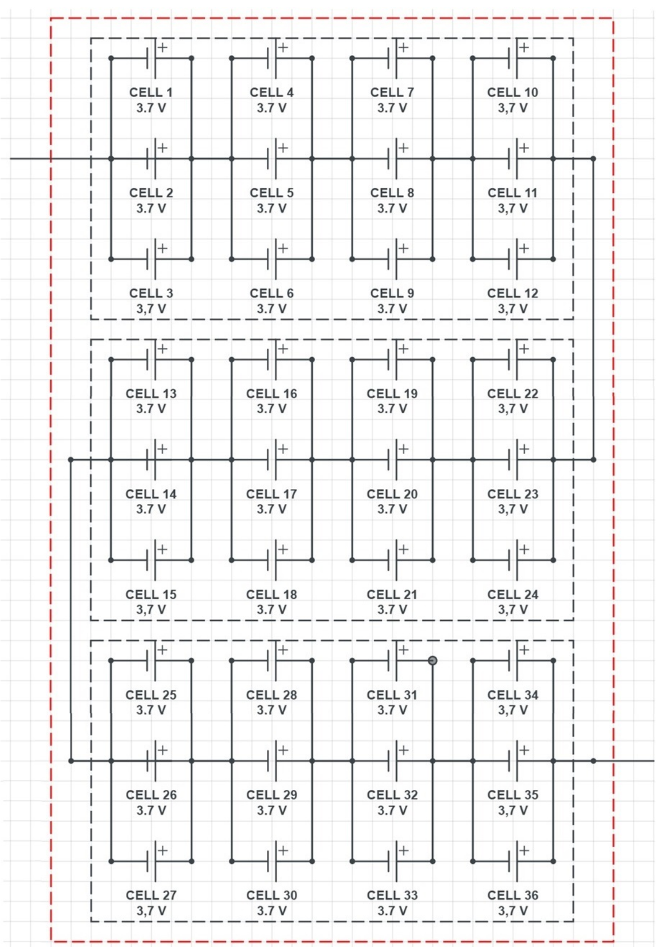

Figure 5. *Module 0* internal circuit representation.

The second module, *Module A*, contains 24 cells arranged in a 2p12s configuration, also featuring a 44.4 V nominal voltage. Its circuitry differs from *Module 0* by having three resistors less for each *Lot A*, one for each parallel branch.

Battery Module Case Numerical Model

The external case of *Module 0*, with a partial view of the internal cells, is displayed in Figure 6.

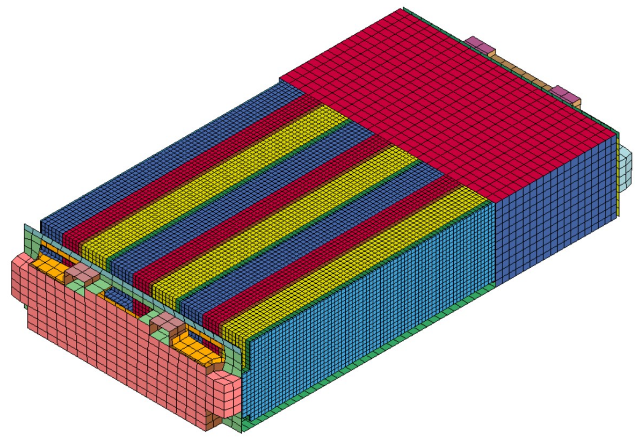

Figure 6. Battery *Module 0* external case.

Both modules casings measure 104.7 mm $\times$ 586.8 mm on the plane parallel to the cell longitudinal section, while their dimension along the third axis are 313.0 mm for *Module 0* and 208.7 mm for *Module A*, respectively. The light blue layer in Figure 6 represents the pouch bag. The protective structure is made of AA2024-T3 aluminum alloy, chosen for its lightweight material property and mechanical strength, which help to protect the cell from impact and confine the thermal runaway events, enabling a safe landing and a consequent evacuation of the cabin.
AA2024-T3 is characterized by a yielding stress σ_Y of 374.1 MPa (Ref. 10), a specific heat capacity *HC* of 900 J/(kg K) and a thermal conductivity *TC* of 210 W/(K m) (Ref. 8). The top (red), bottom (green) and the side plates (blue) of the battery case are connected through shared nodes. the front (pink) and the rear-end plates (cyan) are connected through rigid node-to-node spotweld connections.

Module 0 Normal Discharge Simulation

To verify the electrical connections between the battery layers and the current distribution in the model, discharging simulations were performed on *Module 0* and *Module A*. The first case is proposed hereafter.
The battery Module is connected to an external resistor under normal discharge. All the battery layers are connected with isopotential connections. The resulting current density is presented in Figure 7.

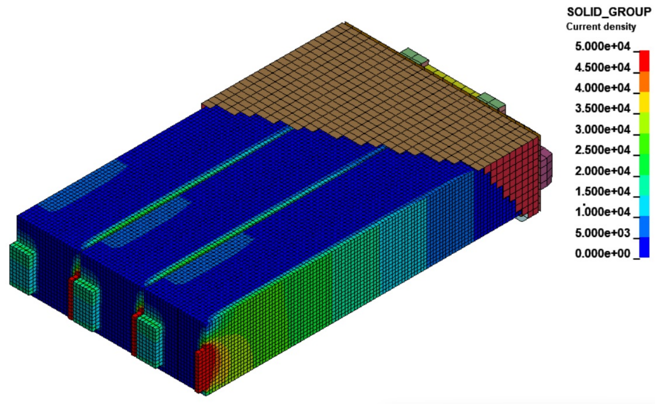

Figure 7. ***Module 0*** **battery current density simulation.**

A consistent current density distribution is observed: all three *Lots 0* exhibit a similar pattern, with localized peaks at the connectors, which is caused by the current concentration at the narrowed current collectors. The cathode collector layer exhibits the highest current density values due to its lowest thickness compared to the other layers and can therefore be selected as a reference for all the other layers distribution. A linear increase in current density in the battery is expected and confirmed, as the cathode current collector is in direct contact along one longitudinal face with the cathode, and a rise in current density near the connector region appears reasonable.

On the other hand, Figure 8 illustrates the voltage drop across the battery module. As indicated by the colors distribution, a voltage rise is imposed across the separators layers, defining four main regions that appear to exhibit constant distinct potential levels. In reality, a resistive effect and an associated voltage drop occur in each individual layer; however, due to their very low resistivity, this effect is not visually recognizable in the normal discharging case.

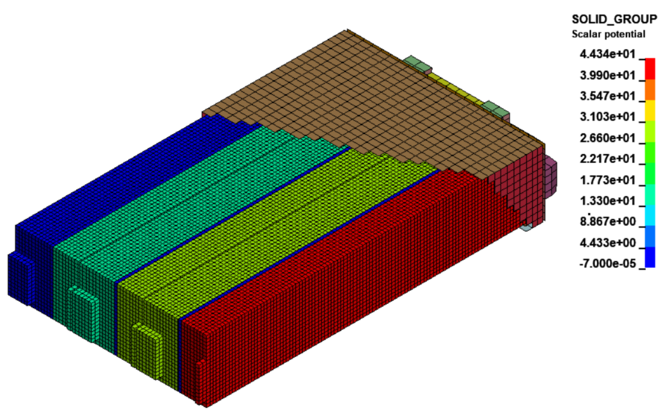

Figure 8. ***Module 0*** **battery voltage drop simulation.**

The same procedure was also applied to verify the correct electrical behavior of *Module A*, gathering similar results.

Battery Pack Assembly

Once the multi-physics models of the battery modules were completed, the entire battery pack was assembled for its electric connections. Its circuitry is represented in Figure 9.

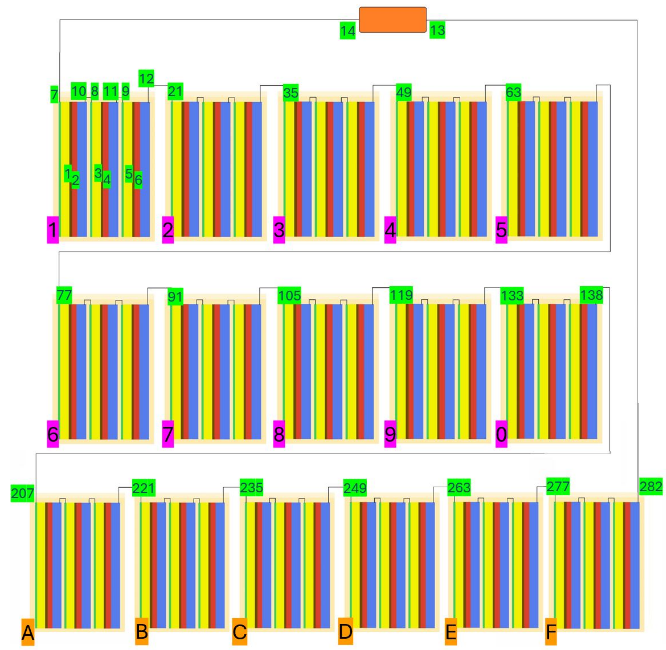

Figure 9. Battery pack circuitry connections.

A total of 10 *Module 0* batteries is selected, labeled from 1 to 0 in a top-left to bottom-right sequence and with their Module ID colored in violet. The assembly bottom row includes 6 *Module A* batteries, labeled from A to F and similarly highlighted in orange. For the sake of simplicity, only *Module 1* on the upper left corner shows the isopotential IDs used for connections within the module, as represented in Figure 9 with green numbered labels. Each of them corresponds to an isopotential voltage condition, and can be interpreted as an electrical terminal associated with a specific battery layer or surface.
Since the battery pack will be placed in three different locations, different battery arrangements will be designed. Nevertheless, the electrical layout is the same, as the battery configuration does not change in terms of total energy and power required during the mission.
Table 4 lists the connections between the isopotential node sets in the entire circuit. Only the internal module connection associated with *Module 1* are provided in detail, as the remaining ones follow a same iterative scheme. The first column provides the *connection* ID number, while the third one indicates the sets of nodes being linked together.
The last row defines the isopotential reference for the entire battery pack, corresponding to a direct connection to the ground (denoted as *GND*). All the connecting wires are assumed to be ideal conductors, i.e., with zero resistivity.

Table 4. Battery electric terminal connections.

N°	Function	Linked Node Sets	ΔV
1	Conn. to *R_EXT*	7 - 14	-
2	Connecting wire	10 - 8	-
3	Connecting wire	11 - 9	-
4	Voltage drop	1 - 2	14.8 V
5	Voltage drop	3 - 4	14.8 V
6	Voltage drop	5 - 6	14.8 V
7	Connecting wire	12 - 21	-
...	...	...	...
97	Conn. to *R_EXT*	282 - 13	-
98	Absol. voltage *(GND)*	282	-

Once the initial transient phase ends, a capacitor behaves like an open circuit. As a result, R1 and R22 can be considered as resistors combined in series (see Figure 4). Based on internal calculations supported by experimental data, the total internal resistance of the battery pack $R_{int,total}$ is calculated in Equation (8):

$$R_{int,total} = 10R_{eq,Mod0} + 6R_{eq,ModA} = 87.932 m\Omega. \quad (8)$$

The nominal voltage of entire battery pack is computed in Equation (9):

$$V_{total,pack} = (10+6) \times V_{module} = 16 \times 44.4V = 710.4V. \quad (9)$$

External resistor model and circuit validation

Once the battery design was concluded, the focus shifted to the propulsive system and powertrain. All the circuitry components, except for the battery itself, were condensed in one single simplified element, referred to hereafter as the *external resistance R_EXT*. This strategy is justified by the fact that the powertrain is not relevant to the present crashworthiness study. *R_EXT* is modeled as a simple solid box 100 mm in length, with a rectangular cross-section of 10 mm $\times$ 20 mm.

For each flight phase, a specific amount of power is required to be delivered by the battery pack. As a result, both voltage and current vary significantly during the mission. As a result, in crash scenarios, there are no voltage and current values that can be generalized for the entire mission. Additionally, the resistivity value of *R_EXT* must be also adapted case by case. Figure 4 showed a simplified verification circuit for a single cell. The same scheme can be scaled to the full battery pack in order to simulate different flight conditions.

As an initial case study, the first crash simulation is set to occur during the cruise phase, which is one of the most stable flight conditions in terms of aircraft attitude and power fluctuations. During cruise, the required power for the motors and propellers is $P_{cr} = 259\,500 W$, obtained from internal performance analyses. Equation (10) describes a power balance condition that can be written for the entire circuit as:

$$P_{batt} - P_{batt,res} - P_{cr} = 0, \quad (10)$$

which, if readapted, expands to Equation (11):

$$-R_{int,total} i^2 + V_{batt} i - P_{cr} = 0. \quad (11)$$

Solving this quadratic equation in the unknown current i yields two solutions:

$$i_1 = 383.5\,\text{A} \quad (12)$$

$$i_2 = 7695.5\,\text{A} \quad (13)$$

The second solution is discarded as it would imply an unrealistic scenario in which the battery becomes the mayor voltage consumer, while the external resistor acts as the battery's internal resistance. Hence, the correct value for *R_EXT* is provided in Equation (14):

$$R\_EXT = \frac{P_{cr}}{i_1^2} = 1.765\ \Omega, \quad (14)$$

with a corresponding voltage drop (Equation (15)):

$$V_{EXTRES} = \frac{P_{cr}}{i} = 676.7V. \quad (15)$$

These analytical results were compared with numerical simulations. Figure 10 presents the resulting voltage distribution across the modules.

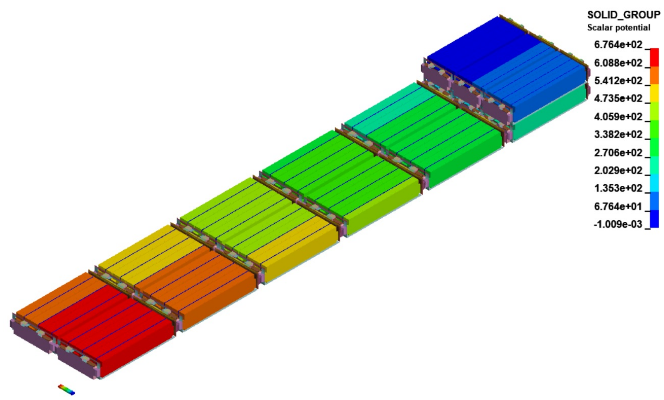

Figure 10. Cruise phase: simulated voltage distribution.

As shown, the maximum simulated voltage reaches 676.4 V, matching with the analytical prediction of 676.7 V derived in Equation (15). The battery modules also visually confirm the voltage gradient: starting from *Module F*, colored in blue and connected to ground, up to *Module 1*, in red, which exhibits the highest potential.

This calibrated configuration can be now used to simulate other flight phases. Although the required power varies depending on the flight condition (e.g., hover, transition), simulations showed that using the same model while keeping *R_EXT* unchanged does not significantly affect the voltage drop compared to the analytical results. For instance, in the hover condition, typically the most demanding in terms of power, the deviation remains within 6% of the expected value, confirming the robustness of the model.

Battery Placement on the Subfloor Structure and Boundary Conditions Definition

Once the battery pack definition was finalized, it was installed on an in-house developed energy-absorbing subfloor.

Figure 11 presents the final configuration. To reduce computational cost, symmetry boundary conditions are applied with respect to the longitudinal YZ plane; consequently, only half of the structure undergoes simulations.

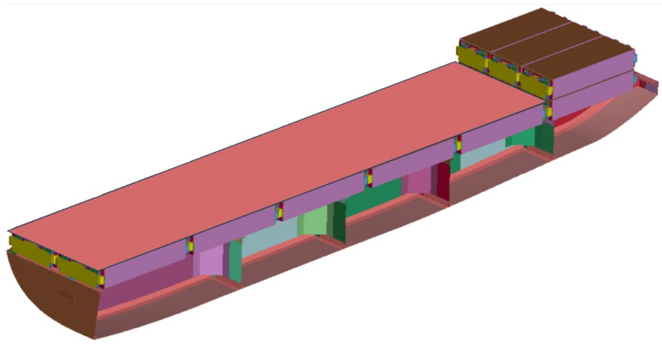

Figure 11. Battery and mass placement on the subfloor.

Figure 12 displays the internal subfloor structure, which is composed of two longitudinal members and four transverse ones. All intersections include oblique elements to enhance the energy absorption capability of the structure.

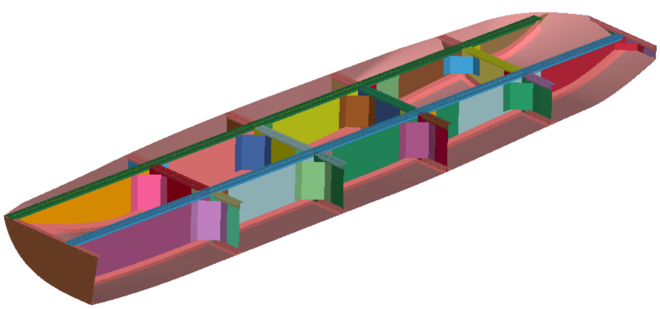

Figure 12. Subfloor structure (upper surface removed).

The subfloor assembly is composed of AA2024-T3 aluminum alloy, with sheet thicknesses ranging from 0.8 mm to 1.2 mm depending on the specific structural component. The design is inspired by a single element energy-absorbing subfloor component previously analyzed by Surini and Nicolotti (Ref. 11). For simplicity, a piecewise linear plasticity model is used to follow the quasi-static curve of AA2024-T3 in the FAA report (Ref. 12).

In addiction to the already presented components, a distributed rigid mass of 400 kg, modeled by a rigid thin plate, colored in pink, was placed on top of the larger modules (as represented in Figure 11). This is necessary to simulate the presence of the occupants and their seats. It is worth noting that the present model does not include the supporting pylons for the cabin and wings structures, which are assumed to be decoupled from the subfloor for the purpose of this simplified study.

The complete model consists of approximately 2 864 000 elements, of which 2 066 000 are solid elements, 795 000 shell elements and 3 000 beam spotwelds elements. All the elements in the model employ a fully integrated formulation to enhance numerical stability during dynamic simulations.

Both the thermal and electromagnetic solvers operated using a fixed timestep of $2.5 \cdot 10^{-6}$ s, which ensured stable results without divergence issues. Additionally, a convective thermal model representing a forced-air cooling system was implemented to simulate the coolant behavior and enable heat dissipation from the battery pack due to Joule heating within the battery layers, thereby preventing temperature rises that could be misinterpreted as thermal runaway events. The surface to surface contact card used in the simulation also includes thermal interactions for a more realistic solution.

The entire structure is subjected to gravity loading, and the initial vertical impact velocity is set at 9.14 m/s (30 ft/s), in accordance with the emergency landing conditions prescribed in *FAR 27-562* (Ref. 13). A node located on the lower surface of the rigid mass was monitored to evaluate vertical decelerations during the crash event, with the signal post-processed with a CFC 180 filter to ensure consistency with regulatory guidelines.

The subfloor selected for the test was intentionally designed to be stiffer than typical configurations, in order to subject the battery pack to more severe deceleration loads among all evaluated designs. Demonstrating that the battery behavior does not present significant internal damage or the occurrence of short circuits under such demanding conditions provides confidence that the risk of failure under lower inertial loads is significantly reduced. As shown in Figure 14, the subfloor deceleration reaches an average of approximately 50 g, which exceeds the typical values observed in existing helicopters designs, with an initial peak of 65 g. The reason for testing under such extreme conditions is further supported by experimental data from battery drop tests conducted at from *NASA Langley Research Center* (Ref. 14). In that occasion, a battery at 0% State of Charge was dropped onto a rigid surface at an impact velocity of approximately 17 m/s, while supported by a honeycomb structure at its case base. The crash event resulted in a peak deceleration of 80 g; however, the battery showed no significant physical damage and no evidence of localized short circuit events.

RESULTS

The simulation for the first case under study, which presents the battery installed upon the subfloor structure, took 68 hours to complete and covered a simulated time interval of 0.0235 seconds.

Mechanical aspects

The results discussion begins with an analysis regarding mechanical deformations, aimed at identifying potential contact or penetration between battery layers, which may lead to the initiation of a thermal runaway event. Additionally, local deformations are being evaluated to assess the post-crash condition of the ESS, monitoring the plastic strain in the battery

layers to determine if material limits for safe operation have been exceeded.
Figure 13 shows the deformation of the entire assembly after 0.0235 s and highlights how the subfloor structure has deformed during the crash event. The deceleration graph of the occupants' distributed mass is provided in Figure 14.

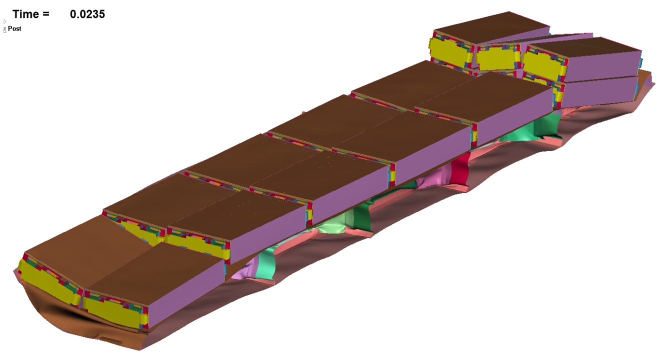

Figure 13. Subfloor Deformed Shape at 0.0235 s.

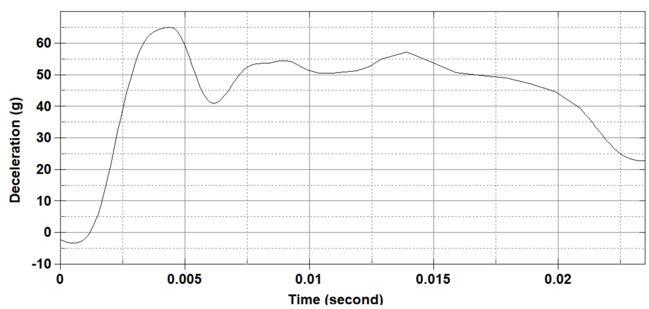

Figure 14. Subfloor Deceleration Crash Pause.

Figure 15 illustrates the effective plastic strain in the entire structure, with an upper limit set to 0.1 (equivalent to 10%).

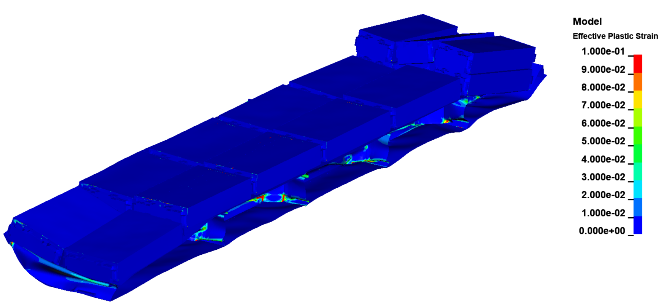

Figure 15. Effective Plastic Strain at 0.0235 s.

Folds in the thin energy-absorbing components are clearly visible in proximity of the spotwelds. Local spikes can be observed at intersections between diagonal elements and the crossing stiffeners. However, no significant damage is visible on the external casing of the battery modules.
Figure 16 shows the bottom-up view of the five battery layers, enabling an evaluation of the local deformations. No plastic deformation or damage was observed on the separator membrane, indicating that the battery is not expected to undergo immediate thermal runaway right after the crash event. This outcome is attributed to the developed design, for the battery layers are oriented perpendicular to the deceleration direction.

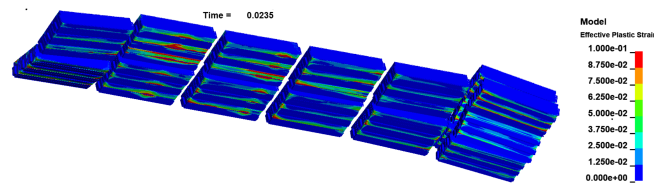

Figure 16. Battery Layers' Plastics strain at 0.0235 s (Bottom Side View).

Analysis shows that the most severely deformed battery modules are those positioned at the center. This is attributed to the weaker structural supports at the edges, which impose lower deceleration levels on the outer modules, resulting in reduced mechanical damage in those regions. Although the edge modules experience lower plastic strain, some localized peaks are observed in the cathode layers, significantly exceeding the material's plasticity limits. Consequently, the post-impact condition of all cells makes them unusable due to compromised structural integrity. It is also noted that non-uniform cathode layer thickness may lead to the formation of local hotspots during repeated cycling, potentially resulting in internal short circuits.

Electric aspects

From an electric point of view, the total voltage of the battery pack does not exhibit an unexpected variation from its initial value. As illustrated in Figure 17, battery modules move independently during the crash event; however, no electrical short circuits or contact between anode and cathode layers were detected.

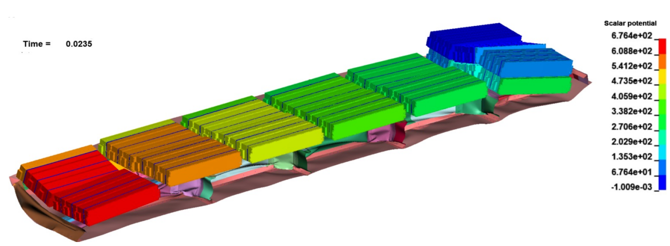

Figure 17. Electric voltage during crash.

Therefore, thermal runaway is unlikely to occur in this specific crash event. However, in a more server crash involving higher impact velocity, excessive mechanical deformation or deceleration may damage the separator sheet and induce an internal short circuit and thermal runaway. Furthermore, if an external short circuit occurs due to damage of electrical connections, resistive heating (Joule effect) may cause thermal runaway in absence of adequate heat dissipation systems.

Thermal aspects

Figure 18 displays the temperature distribution within the subfloor structure at the same time instant as the mechanical and electrical analyses. The colormap values are constrained between 293.15 K and 308.15 K to enhance readability.

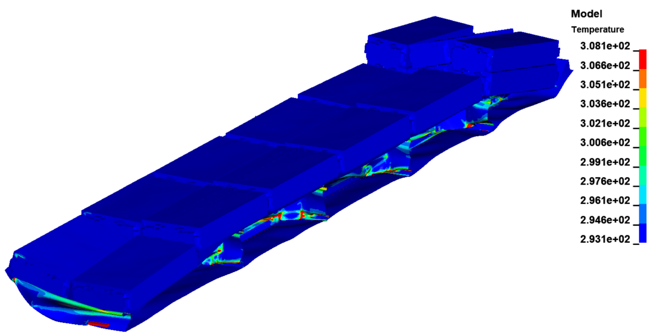

Figure 18. Temperature scalar field at 0.0235 s.

As expected, the subfloor's energy-absorbing components have deformed under inertial loads, resulting in a noticeable temperature increase. The lower surfaces of the external battery casings exhibit little increments in temperature caused by inertial loads generated by the internal layers, while the upper sections remain close to the room temperature of 293.15 K.
A more detailed view of the thermal response of *Module A* batteries is provided in Figure 19. The visualization range limits have been restrained to 293.0-295.0 K.

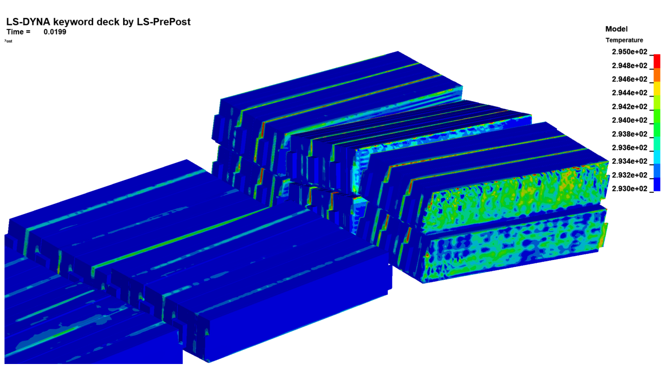

Figure 19. *Modules A* internal layers temperature field.

The temperature distribution confirms that the deformation observed in Figure 15 affects the cathode collector layer, resulting in localized increments of temperatures. At the same time, the convective cooling system appears to function effectively, keeping the battery temperature close to the initial conditions: it is worth noting that the temperature increase remains limited to only 2 $°C$. A higher temperature rise is observed in *Module A* if compared to *Module 0*. This is attributed to the fact that the smaller *Module A* exhibits higher internal resistance than the larger *Module 0*; hence, when connected in series, more heat is generated in the smaller module. Therefore, under this conditions, the thermal effect is not expected to trigger a thermal runaway.

DISCUSSION

A fully-coupled thermal-electrical-mechanical simulation has been performed to evaluate battery safety in the event of vertical crash of an eVTOL aircraft. The multi-physics analysis framework has enabled the simulation of battery thermal runaway events triggered by structural impact loading.
The advantages of this methodology include:

1. **Capturing the actual physics leading to thermal runaway events within the battery**: The representative battery module include realistic thermal, electrical, and mechanical properties for the battery internal materials. The internal configuration of the battery cells is also replicated in the model. These features allow for the simulation of the physical mechanisms that lead to thermal runaway.

2. **Evaluating the subfloor and battery pack performance**. Since the modules are electrically connected and thermal contact is established between the battery and the surrounding structural components, the system is capable of simulating heat exchange and assessing the thermal runaway behavior at both module and pack level.

3. **Solving thermal and electric problems**: The multi-physics battery simulation model accurately simulates battery heat dissipation, making it suitable for the design of thermal management systems. Additionally, the electric circuit simulation supports the design and verification of battery electrical circuitry.

The main limitations of this approach are:

1. **The conceptual model has limited accuracy in geometry and material properties**: The battery and subfloor multi-physics simulation is based on an in-house developed generic eVTOL model. The geometry configuration and material data are derived from literature sources. For an accurate prediction of battery thermal runaway during a subfloor drop test, the simulation model must closely reflect the actual geometry of the system in service. Furthermore, realistic material properties for both the subfloor and the battery system are essential. To enhance simulation fidelity, the material models should incorporate strain-rate sensitivity and temperature-dependent behavior.

2. **Modeling effort and computational cost**: The multi-physics simulation requires advanced skills in creating a stable and representative model. Significantly high computational resources are required as well. A time penalty of approximately two to three times is observed compared to mechanical-only simulation; this is added to a penalty of up to seven times in terms of simulation file size, which increases memory and storage requirements.

3. **Mesh size limitations**: In the current framework, the entire battery pack and subfloor structure are simulated together. This requires the use of relatively large mesh elements for the battery, as smaller elements would make the simulation computationally prohibitive. However, fine meshes are desirable in order to capture the deformation patterns and complex physics leading to thermal runaway. Future work could explore use a multi-scale approach, using fine mesh size for detailed cell models, and coarser mesh elsewhere is used when deformation or deceleration is negligible.

The insights obtained during the model development and the results of the numerical simulations provide a first critical evaluation regarding the choice of installing the entire battery pack on the subfloor structure, as opposed to alternative placements. The advantages and disadvantages of the *battery-on-the-subfloor* configuration are hereby summarized.

Identified advantages:

1. **Efficient load distribution**: the configuration allows for a balanced distribution of the battery modules over the energy-absorbing subfloor, aiming for a design development similar to a conventional helicopter design;

2. **Reduced fuselage reinforcement on pylons and overhead**: the absence of battery mass above the passengers cabin reduces the need for additional structural reinforcement in the upper fuselage, enabling a lighter design;

3. **Simple design process**: subfloor structures are well-known design assemblies with decades of development experience, leading to an easier ballast integration and structural assessment;

4. **Center of Gravity location**: compared to other layouts, the subfloor configuration has a minimal impact on the eVTOL CoG overall position;

5. **Efficient maintenance due to battery modules accessibility**: given that the state-of-the-art battery modules typically require replacement every 5̃00 flight hours, or approximately three months if assuming eight flights per day, placing the batteries on the subfloor allows for faster access, reduced maintenance time and simple replacement procedures.

Identified disadvantages:

1. **Reduced cabin vertical clearance**: locating the battery pack over the subfloor decreases the available vertical space by approximately 12 cm (5 inches), potentially affecting passengers comfort or causing redesigning of the entire cabin, deviating from traditional rotorcraft-inspired fuselage profiles. Moreover, the subfloor depth must be ulteriorly increased to properly absorb the battery ballast mass;

2. **Occupant proximity to the energy systems**: while regulatory standards can be successfully met, the placement of high-energy systems directly beneath passengers introduces critical safety concerns in the event of a harder crash. Even if thermal titanium insulation cases are implemented, the proximity of the battery system may not be enough to limit exposition to fire or explosions;

3. **Increased wing loading**: in this specific configuration, the wings are not structurally counterbalanced by any energy system installed in the wings, as would occur with wing-integrated battery modules. Consequently, wings structures must withstand greater stresses induced by lift, potentially leading to increased structural mass, despite this aspect remains highly design-dependent.

4. **Heavier subfloor structure**: on the same wavelength, concentrating the mass in the lower fuselage requires a reinforced subfloor to manage the increased structural demands.

CONCLUSIONS

1. The eVTOL sector is rapidly growing, yet current standards still lack clear and precise regulations regarding crash dynamics and the effects of thermal runaway are still lacking, highlighting the need for further research.

2. A fully coupled mechanical-thermal-electrical simulation model of a single battery cell has been developed to predict the battery thermal runaway.

3. A realistic battery module model based on a Randles circuit was developed. The model account for internal resistances change in the representation and improved the reliability of the simulation.

4. The subfloor and battery crash simulations model shows that when the battery pack is installed on the top of the subfloor, several layers suffer irreversible damage; however, no visible direct contact occurs between anodes and cathodes, preventing short circuits during the impact event. No immediate thermal runaway is predicted under our loading case.

5. An alternative configuration involving battery placement inside the wings is being explored; although this design

introduces additional complexity, it may enhance passive safety if the wings are designed to detach in a controlled way, allowing inertial loads to directly dissipate on ground instead of through the fuselage structural pylons; a third configuration considers relocating the batteries behind the passengers, but this choice introduces potential challenges in maintaining center of gravity limits and requires an assessment of new deceleration profiles to ensure compliance with safety standards.

FUTURE WORK

At the time of writing, the second phase is already underway, with numerical simulations currently being conducted to extract further insights from the battery-inside-the-wings configuration. Once finalized, a comparative analysis - especially regarding total mass variation - will be carried out.
From an external perspective, installing the ESS inside the wings may appear more rational; however, this choice results in greater design complexity and potentially heavier structural components. A key aspect in this innovative configuration led its basis in the ability to design a controlled detachment of the wings during crash scenarios. In that case, the inertial loads generated by the battery modules are directly transferred to the ground, and no forces are transmitted to the structural pylons or the fuselage itself. Although the electrochemical response in such impact conditions may be more critical, appropriate containment measures, such as thermal shielding and venting systems, can significantly reduce the risks of fire, gas leakage and explosions. With proper design considerations, this innovative solution may offer better advantages if compared to the configuration approach discussed previously.

The third phase of the project focuses on a revised layout of the battery modules installed on the subfloor, but positioning them entirely behind the passenger cabin. This new configuration increases the physical separation between the ESS and the occupants, potentially enhancing safety. Nevertheless, some concerns arise regarding the final CoG location and the consequent implications to respect such performance constraints. In this case, a stiffer subfloor must be designed and installed in the rear fuselage, but while this solution implies structural reinforcements,it offers one notable advantage: the absence of human acceleration constraints allows for higher tolerable impact decelerations, eventually improving the system's crashworthiness.

Authors contact:
Luca Riva: luca11.riva@mail.polimi.it
Alessandro Giustina: alessandro.giustina@polimi.it
Marco Anghileri: marco.anghileri@polimi.it
Stefano Dolci: sdolci@gmu.edu
Cing-Dao Kan: cdkan@gmu.edu
Leyu Wang(Corresponding Author): lwang28@gmu.edu

REFERENCES

1. Nathen P., Bardenhagen A., Strohmayer A., Miller R., Grimshaw S., Taylor J., *Architectural performance assessment of an electric vertical take-off and landing (e-VTOL) aircraft based on a ducted vectored thrust concept*, April, 2021.
2. European Union Aviation Safety Agency, *Special Condition for small-category VTOL-capable lift*, 1^{st} version, July, 2019.
3. European Union Aviation Safety Agency, *Special Condition for small-category VTOL-capable lift*, 2^{nd} version, June, 2024.
4. Federal Aviation Administration, U.S. Department of Transportation, *Advisory Circular No: 21.17-4. Type certification - Powered-lift*, June, 2024.
5. Littell, J. D., Gardner, N. W., Ellafrits, S. A.,*Dynamic Testing of eVTOL Energy Storage Systems: Literature Review and Path Forward*, January, 2023. NASA/TM–20220015117.
6. *NCM 712 by LG Chem: E66A and E78 battery cells in detail*, March, 2021. URL: https://pushevs.com/2021/03/30/ncm-712-by-lg-chem-e66a-and-e78-battery-cells.
7. *VolksWagen ID 4 82kWh Battery*, February, 2024. URL: https://www.batterydesign.net/vw-id-4-82kwh-battery.
8. L. Wang, C. Ling, C. D. Kan, C. Yang, *A coupled thermal-electrical-mechanical analysis for lithium-ion battery*, Journal of Micromechanics and Molecular Physics, Center for Collision Safety and Analysis, Fairfax, VA, February, 2022.
9. C. Ling, L. Wang, C. D. Kan, C. Yang, *Thermal–Electrical–Mechanical Coupled Finite Element Models for Battery Electric Vehicle*, Center for Collision Safety and Analysis, Fairfax, VA, August, 2024.
10. J. D. Seidt, C.-K. Park, M. Buyuk, R. L. Lowe, L. Wang, K. S. Carney, P. Du Bois, A. Gilat, C.-D. Kan, *An Experimental Investigation of the Influence of the State of Stress on the Ductile Fracture of 2024-T351 Aluminum*, Journal of Engineering Materials and Technology, Vol. 144, No. 4, pp. 041006, August 2022.
11. Surini, A., Nicolotti, M., *Analisi sperimentale e numerica della sicurezza passiva di un moderno sottopavimento di elicottero*, Master's Thesis, Appendix A, page 17, Politecnico di Milano, April, 2011.
12. C.-K. Park, K. Carney, P. Du Bois, C.-D. Kan, D. Cordasco, *Aluminum 2024-T351 Input Parameters for *MAT_224 in LS-DYNA Part 4: Ballistic Impact Simulations of a Titanium 6Al-4V Generic Fan Blade Fragment on an Aluminum 2024 Panel Using *MAT_224 in LS-DYNA*, DOT/FAA/TC-19/41, P4, Final Report, Federal Aviation Administration, September 2021.

13. Federal Aviation Administration, *§ 27.562 Emergency landing dynamic conditions*, Federal Register, Rules and Regulations, Vol. 54, No. 217, page 47318, November, 1989.

14. J. D. Littell, *Overview of NASA's Impact Testing of Energy Storage Systems Research: A Summary of Phase 1 and 2 Results*, Aerospace Ecosystem Working Group, NASA Langley Research Center, Structural Dynamics Branch (D322), November 5, 2024.